

Topological two-dimensional Floquet lattice on a single superconducting qubit

Daniel Malz^{1,2,*} and Adam Smith^{3,*}

¹Max Planck Institute for Quantum Optics, Hans-Kopfermann-Straße 1, D-85748 Garching, Germany

²Munich Center for Quantum Science and Technology, Schellingstraße 4, D-80799 München, Germany

³Department of Physics, TFK, Technische Universität München, James-Franck-Straße 1, D-85748 Garching, Germany

Previous theoretical and experimental research has shown that current NISQ devices constitute powerful platforms for analogue quantum simulation. With the exquisite level of control offered by state-of-the-art quantum computers, we show that one can go further and implement a wide class of Floquet Hamiltonians, or time-dependent Hamiltonians in general. We then implement a single-qubit version of these models in the IBM Quantum Experience and experimentally realize a temporal version of the Bernevig-Hughes-Zhang Chern insulator. From our data we can infer the presence of a topological transition, thus realizing an earlier proposal of topological frequency conversion by Martin, Refael, and Halperin. Our study highlights promises and limitations when studying many-body systems through multi-frequency driving of quantum computers.

I. INTRODUCTION

Noisy intermediate-scale quantum (NISQ) computers may not yet offer fully fault-tolerant quantum computing facilities, but they nevertheless constitute a versatile experimental platform with the potential for fundamental research, small-scale computation or quantum simulation [1]. The typical model of a quantum computer is that of a quantum circuit, which is a sequence of gates applied to the qubits. A small set of gates is sufficient to in principle perform any computation on the quantum computer [2]. This allows digital simulation of many-body quantum mechanics, with important applications in quantum chemistry [3, 4]. In principle, the time-evolution of any many-body quantum systems can be simulated by applying a Trotterization, which turns the continuous time evolution into a local quantum circuit [5]. This approach to quantum dynamics has now been benchmarked for a range of different models on existing quantum computers [6–9].

The abstraction into quantum circuits hides the complexity of the underlying platform. In superconducting circuits, the currently leading technology, the set of available gates correspond to a set of carefully calibrated microwave pulses that are applied to its input ports, and a quantum circuit is the concatenation of these pulses [10]. In the absence of driving, the continuous evolution of a superconducting-qubit quantum computer is similar to a disordered Bose-Hubbard model [11], a fact that suggests that these devices may also offer exciting direction in analogue quantum simulation. This perspective has been explored in a series of theoretical and experimental works [12–15]. If the intrinsic many-body nature of quantum computers is combined with the capacity to apply essentially arbitrary drives, they may serve also as powerful analogue quantum simulators for very large classes of *time-dependent* Hamiltonians.

The evolution under time-dependent Hamiltonians is incredibly rich and exhibits many novel phenomena, even at the level of individual qubits. A particular example is the temporal topological transition that occurs in the presence of

quasiperiodic driving, theoretically predicted by Martin, Refael, and Halperin in 2017 [16]. Using a Floquet treatment of the driven qubit, the dynamics is related to the properties of a two-dimensional lattice model, the Bernevig-Hughes-Zhang (BHZ) Chern insulator [17]. As a function of time, the driven qubit explores the whole Brillouin zone, which causes the work done by the two drives to be quantized and proportional to the integer Chern number, which is determined by the parameters in the drives. Recently, temporal topology has been classified, analogously to the classification of topological insulators [18], and extension to larger systems, such as spin-resonator systems [19], or two-qubit systems with interactions [20] have been proposed. While quasiperiodic driving typically maps to systems without boundary, one can in principle also introduce boundaries through quantum feedback [21].

In this work we experimentally demonstrate this temporal topological behaviour of a single-qubit system on an existing quantum device, using continuous driving, implemented with the fine-grained access offered by QISKit pulse [22]. Choosing a specific driving with two incommensurate frequencies, we observe a topological transition in the temporal dynamics of the qubit, finding good agreement with simulations.

Motivated by this experiment, we theoretically derive the class of Hamiltonians that can readily be implemented on state-of-the-art quantum computers. As one concrete example, this offers an exciting perspective to study strongly interacting Floquet systems [23–27] with an exquisite level of control. The high-level site-specific control as well as high-fidelity single-site readout confers quantum computers certain advantage over other quantum simulators based on light [28] or ultracold atoms [29], making them ideally suited for the analogue quantum simulation of generic many-body time-dependent Hamiltonians.

II. THEORETICAL DESCRIPTION

In quantum computers based on superconducting transmon-like qubits [30, 31], the Hamiltonian describing a single qubit can be cast in the form of a Duffing oscillator with driving

$$H(t) = \omega_0 a^\dagger a + U a^\dagger a^\dagger a a + (a + a^\dagger) D(t). \quad (1)$$

* Both authors contributed equally.

The qubit frequency is denoted ω_0 and U quantifies the anharmonicity that separates the lowest two levels that define the qubit from the higher levels of the superconducting circuit. The ideal drive signal is parametrized as [22]

$$D(t) = \frac{\Omega_{\max}}{2} \operatorname{Re} \left[e^{i(\omega_0 + \Delta_c)t} d(t) \right], \quad (2)$$

where Ω_{\max} denotes the maximum Rabi frequency attainable in the system, and we choose the detuning $\Delta_c = 0$. Anticipating our later interpretation as a spin-1/2 particle in a time-dependent field, we parametrize the dimensionless drive shape $d(t) \in \mathbb{C}, |d(t)| \leq 1$ in terms of the dimensionless magnetic field $\tilde{h}_+(t) = \tilde{h}_x(t) + i\tilde{h}_y(t)$

$$d(t) \equiv \tilde{h}_+(t) \exp i\phi(t), \quad (3)$$

with time-dependent phase

$$\phi(t) = -2\Omega_{\max} \int_0^t \tilde{h}_z(t') dt'. \quad (4)$$

In order to treat the system as a qubit, the maximum drive strength needs to be much weaker than the anharmonicity $\Omega_{\max} \ll U$. Assuming this is fulfilled, applying a rotating-wave approximation and passing into a frame rotating with the qubit frequency, we rewrite Eq. (1) as

$$H_{\text{qubit}}(t) = \frac{1}{2} \sigma_- (h_x(t) + i h_y(t)) e^{-2i \int_0^t h_z(t') dt'} + \text{H.c.}, \quad (5)$$

where we have now introduced the dimensionful magnetic field $\vec{h}(t) = \Omega_{\max} \tilde{\vec{h}}(t)$ and the spin lowering operator σ_- . If we pass (again) into a rotating frame with respect to the time-dependent Hamiltonian $H_z(t) = -h_z(t)\sigma_z$, the Hamiltonian becomes that of a spin-1/2 particle in a time-dependent magnetic field

$$H_{\text{spin}}(t) = \vec{h}(t) \cdot \vec{\sigma}. \quad (6)$$

Note the subtlety when passing from Eq. (5) to Eq. (6). Instead of changing the qubit frequency in the lab frame, we re-parameterize time by passing into a rotating frame with respect to $H_z(t)$. This constitutes a continuous version of virtual Z gates [32].

III. TOPOLOGICAL FREQUENCY CONVERSION

Given Eq. (6), we can now realize the proposal by Martin *et al.* [16]. We apply the time-dependent magnetic field

$$H(t) = \eta \left\{ \sin(\omega_1 t + \phi_1) \sigma_x + \sin(\omega_2 t + \phi_2) \sigma_y + [M - \cos(\omega_1 t + \phi_1) - \cos(\omega_2 t + \phi_2)] \sigma_z \right\} \quad (7)$$

where $\omega_2/\omega_1 = (1 + \sqrt{5})/2$. We consider the model in the strong drive limit, i.e., $\eta \gg \omega_1, \omega_2$. In this limit we can make a direct connection to the two-dimensional BHZ Chern insulator [17]. We extract the non-trivial Chern number by calculating the work done by each drive.

As a function of M the system shows a crossover from a regime in which the average work done is zero (no topology) to a regime where energy is pumped from one drive to the other at a constant rate Fig. 1.

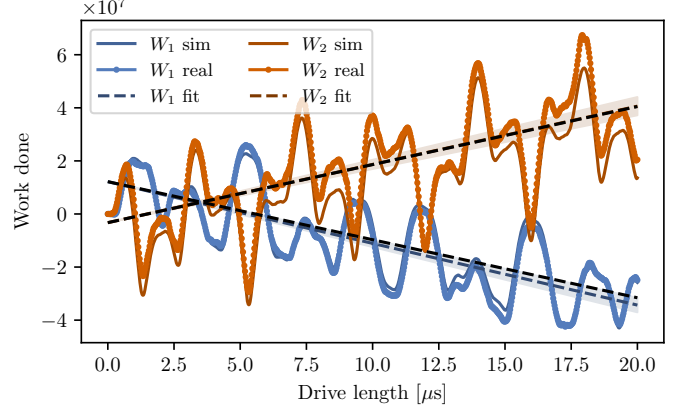


FIG. 1. Work done by the two incommensurate drives, calculated using Eq. (12). The experimental data for $M = 1, \omega_1 = 0.125$ measured at 800 points is compared with a numerical simulation of the same setup. The experimental data is fitted with a line (coloured dashed lines) using least-squares regression, for which the 95% confidence interval for the slope is shown as the coloured region. The expected slope is shown as black dashed lines.

A. Floquet lattice

The connection to the BHZ Chern insulator is elucidated by considering the Floquet construction which relates our time-dependent zero-dimensional system with a two-dimensional lattice Hamiltonian. This is done by considering the following time-dependent states

$$|\Psi(t)\rangle = e^{-iEt} \sum_{\alpha, \vec{n}} \psi_{\vec{n}}^{\alpha} e^{-i\vec{n} \cdot \vec{\omega}t} |\alpha\rangle, \quad (8)$$

where $\alpha = 0, 1$ label the two basis states for the qubit, and $\vec{n} = (n_1, n_2)$, with $n_i \in \mathbb{Z}$ and $\vec{\omega} = (\omega_1, \omega_2)$. The vector \vec{n} is associated with the sites on an infinite two-dimensional square lattice. The time-dependent Schrödinger equation $i\partial_t |\Psi(t)\rangle = H(t) |\Psi(t)\rangle$, can then be written as

$$\begin{aligned} E\psi_{\vec{k}} = & \left\{ \sin(k_x + \phi_1) \sigma_x + \sin(k_y + \phi_2) \sigma_y \right. \\ & \left. + [M - \cos(k_x + \phi_1) - \cos(k_y + \phi_2)] \sigma_z \right\} \psi_{\vec{k}} \\ & - \sum_{\vec{n}} e^{-i\vec{k} \cdot \vec{n}} \vec{n} \cdot \vec{\omega} \psi_{\vec{n}}, \end{aligned} \quad (9)$$

where $\psi_{\vec{k}} = \sum_{\vec{n}} e^{-i\vec{k} \cdot \vec{n}} \psi_{\vec{n}}$, and $\vec{k} = (k_1, k_2)$ with $k_i \in [0, 2\pi]$. The first three terms correspond to the BHZ Chern insulator, discussed in more detail in the Sup. Mat.. The final term is in mixed form and corresponds to a linear potential along the direction $\vec{\omega}$, which can be interpreted as an electric field. In the strong-drive limit, $\eta \gg \omega_1, \omega_2$, this induces a time dependence in the momentum $\vec{k} \rightarrow \vec{k}_0 + \vec{\omega}t$ [16]. Making the substitution for the time-dependent momentum we recover Eq. (7). The dynamics corresponds to the adiabatic evolution of the ground state of Eq. (7) in the Brillouin zone, so long as the gap controlled by M is sufficiently large compared with ω_1 .

B. Chern number

The topological properties of the time-dependent Hamiltonian Eq. (7) manifest as the quantised average energy pumping between the two external drives with frequencies ω_1 and ω_2 . This average pumping rate

$$P = \omega_1 \omega_2 \frac{C}{2\pi} \quad (10)$$

is set by the Chern number of the corresponding BHZ phase. Note that for this quantization to hold we need that the drives are incommensurate and we are in the strong-drive limit.

To experimentally extract this pumping rate we measure the work done by each of the drives. If we first split the Hamiltonian into the two contributions from each drive,

$$H(t) = h_1[\omega_1](t) + h_2[\omega_2](t) + \eta M \sigma_z, \quad (11)$$

then the work done by each drive over a period T is given by

$$W_i(T) = \int_0^T dt \langle \Psi(t) | \frac{dh_i(t)}{dt} | \Psi(t) \rangle, \quad (12)$$

where $|\Psi(t)\rangle$ is the state of the qubit at time t under the time-dependent Schrödinger equation $i\partial_t|\Psi(t)\rangle = H(t)|\Psi(t)\rangle$, where $|\Psi(t=0)\rangle$ is the instantaneous eigenstate of $H(t=0)$. On average we have that [16]

$$\pi \frac{(W_1 - W_2)}{\omega_1 \omega_2 T} = C. \quad (13)$$

We can therefore extract the Chern number by measuring the $\langle dh_i/dt \rangle$ as a function of time and computing by integral in Eq. (12).

C. Experimental details

For our simulation we initialize the qubit in the instantaneous eigenstate of Hamiltonian Eq. (7) at $t = 0$ and then drive the system to realize the evolution under the time-dependent Hamiltonian Eq. (7). In practice, this means that we drive the qubit according to the Hamiltonian in the lab frame Eq. (5), perform state tomography at 800 points in time and then obtain the observables in the rotating frame [corresponding to evolution under Eq. (7)] by applying the rotation

$$\begin{aligned} \langle \sigma_x \rangle_{\text{rotating}} &= \cos \phi(t) \langle \sigma_x \rangle + \sin \phi(t) \langle \sigma_y \rangle \\ \langle \sigma_y \rangle_{\text{rotating}} &= -\sin \phi(t) \langle \sigma_x \rangle + \cos \phi(t) \langle \sigma_y \rangle, \end{aligned} \quad (14)$$

where $\phi(t)$ is given in Eq. (4). When postprocessing the data, we also mitigate some of the errors due to decoherence and measurement by projecting the measured qubit density matrix onto the Bloch sphere. We find that this method of error mitigation improves quantitative agreement with numerical simulations in all cases we considered.

We fix $\omega_2 = \varphi \omega_1$, where $\varphi = (1 + \sqrt{5})/2$ is the golden ratio. Ideally we would like to set the ratio ω_1/η as small as possible. However, due to the finite coherence time $\tau \approx 100\mu\text{s}$

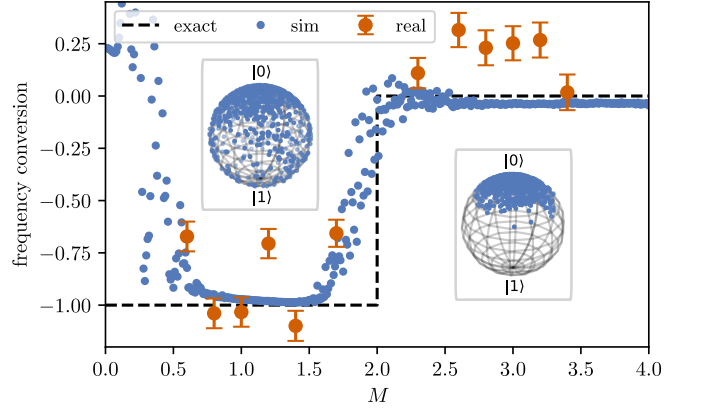


FIG. 2. Experimentally extracted Chern number as a function of M . The Chern number is extracted from the linear least-squares regression fit to the work done by each drive, and using Eq. (13). The error bars correspond to the 95% confidence intervals for the fit. The experimental data is compared against the numerical simulation of the same setup (blue dots) and with the exact value of the Chern number for the corresponding phase of the BHZ model (dashed black curve). Insets show the covering of the Bloch sphere under dynamics for $M = 1$ and $M = 3$, illustrating qualitative differences of the time evolution in each of the two phases $|M| < 2$ and $|M| > 2$.

of the IBM Q device, we must choose $\omega_1^{-1} \ll \tau$. We also choose $\eta = 0.9\Omega_{\text{max}}$ in order to avoid driving transitions to higher excited states. Using numerical simulations we found the best compromise was to choose a total simulation time of $20\mu\text{s}$ and set $\omega_1 = 0.125\eta$, which corresponds to $\omega_1^{-1} \approx 240\text{ns}$. In order to improve the fidelity of our results we start the drive with a linear ramp of the drive frequencies ω_1, ω_2 over a period of 444ns . This reduces transient effects and reduces high-frequency Rabi oscillations seen in the simulation results. The single qubit IBM device we used, codenamed armonk, had qubit frequency $\omega_0 \approx 4.97 \text{ GHz}$ and maximum Rabi frequency $\Omega_{\text{max}} \approx 36.9 \text{ MHz}$.

D. Results

To obtain the work done by each drive [Eq. (12)], we first compute $\langle dh_i(t)/dt \rangle = \vec{d}h_i(t)/dt \cdot \langle \vec{\sigma} \rangle$ from the data. We then perform the integration in Eq. (12) numerically. Figure 1 shows the experimental results for the work done, for the case of $M = 1$. This corresponds to a phase of the BHZ model with Chern number $C = -1$, resulting in an average linear decrease (increase) of W_1 (W_2). The experimental results are in good quantitative agreement with numerical simulations. Furthermore, by fitting a linear curve to this data using least-squares regression, the slope is in close agreement to that predicted by Eq. (13).

Fig. 2 shows the extracted Chern number for a range of values of M , compared against numerical simulations of the same setup as well as the ideal result in the strong-drive limit. We find reasonable quantitative agreement with the simulations. Furthermore, the transition between different phases

with different Chern number is clearly visible in the experimental data. Beyond the extracted value of the Chern number, the qualitative difference between the phases with $|M| < 2$ and $|M| > 2$ is clearly seen by considering the portion of the Bloch sphere covered under time evolution, shown inset Fig. 2. For $|M| < 2$ we observe that the state of the qubit explores the full Bloch sphere under the dynamics of Eq. (7) reflecting that the surface traced by the time dependent state has non-trivial winding around the origin and hence non-zero Chern number. When $|M| > 2$ the state of the qubit is instead restricted to either the north or south hemisphere of Bloch sphere and does not wind around the origin and the Chern number is zero.

While overall, the agreement is good, some outliers appear in the experimental data. By plotting the equivalent of Fig. 1 for those points [cf. SI], we observe that at these points the evolution of the qubit departs from the ideal evolution predicted by the numerics. We thus attributed those points to effects that have not been taken into account in our model, most notably excitations to doubly excited states and decoherence, but it is difficult to tell which effect exactly is responsible.

IV. EXTENSION TO QUBIT ARRAYS

In view of the vast research effort in Floquet matter, the question is pertinent whether the presented scheme generalizes to several qubits. To answer this question we must be aware that the coupling between two qubits can be engineered in many ways, as one can choose between direct capacitive or inductive coupling, or indirect coupling via a resonator [33–37]. Indeed, alternative approaches have been taken by IBM (see, e.g., Ref. [38]) and Google [39], with each implementation having their own (dis-)advantages.

In Appendix A we consider two cases in particular. The first is when both qubit frequencies and their coupling is fixed, which is relevant for the devices developed by IBM. In this case, the coupling has to be engineered with time-dependent driving of the qubits in order to implement resonant processes to second order in the Hamiltonian [40–42]. This technique produces tuneable XZ , YZ , ZX , and ZY interactions, which are used to engineer CR gates [41, 43]. Implementing a similar single-qubit driving as before (Eq. (5)), and passing into a time-dependent reference frame, an effective Hamiltonian of the form

$$H_{\text{int}}^{(2)} = \sum_{\langle ij \rangle} g_{ij}(t) \sigma_z^{(i)} \sigma_z^{(j)} + \text{H.c.} \quad (15)$$

can be derived (Appendix A). On bipartite lattices, a (virtual) rotation of every second spin maps this to either an Ising interaction or (in general anisotropic) XY interactions, making this technique very versatile. A drawback is that the Hamiltonian (15) is obtained to second order in the original Hamiltonian and by neglecting quickly rotating terms. It is thus an approximation and care has to be taken that all the steps in its derivation are valid. Nevertheless, these conditions can usually be fulfilled through careful choice of the driving parameters. It may further be possible to actively counteract unwanted effects from this approximation, analogous to the

DRAG scheme used to improve the fidelity of digital quantum gates [10].

If tuneable interactions are available and the qubits can be brought into resonance [39], an approach pursued (for example) by the Google team, the driving scheme is simplified and one readily arrives at the general spin Hamiltonian

$$H_{\text{array}}(t) = \sum_i \vec{h}^{(i)}(t) \cdot \vec{\sigma}^{(i)} + \sum_{\langle ij \rangle} g_{ij}(t) \left(\sigma_x^{(i)} \sigma_x^{(j)} + \sigma_y^{(i)} \sigma_y^{(j)} \right) \quad (16)$$

with a magnetic field along z that takes the form

$$h_z^{(i)}(t) = h_z(t) + \omega_i(t) - \omega_0, \quad (17)$$

where ω_i are the qubit frequencies and ω_0 is some arbitrarily chosen reference frequency. We note that tuneable qubit frequencies feature in many implementations [44–47], but not in all [48]. In the latter case—of fixed qubit frequencies but tuneable interactions—one option might be to drive each qubit with a far off-resonant drive to induce an drive-strength-dependent AC Stark shift.

When taking into account the second excited state of each qubit, the qubit array Hamiltonian (16) maps to a Bose-Hubbard model with time-dependent hopping and freely tuneable site-dependent drive and disorder. We note that the interpretation as a (time-independent) Bose-Hubbard model has enabled the experimental measurement of microscopic features of the many-body localized phase [14]. Moving to periodically varying hoppings could allow one to study many-body Floquet models and implement quench and ramp experiments from carefully prepared initial states.

V. DISCUSSION

In our initial discussion, we have emphasized the vast promise that time-dependent analogue quantum simulation on quantum computers holds. However, our experiment has also highlighted some of the difficulties that need to be overcome on the way. Concretely, the experimental results shown in Fig. 2 would improve with greater coherence time of the qubit, as this would allow us to reduce the modulation frequencies ω_1 and ω_2 in the Hamiltonian, which in turn improves the strong-driving and adiabatic modulation approximation. This would make the blue simulated dots in Fig. 2 agree better with the step function. Furthermore, the actual results from the quantum computer differ from the simulation, which highlights the need to improve our model of the quantum computer.

Nevertheless, as we have demonstrated, the temporal topological nature of the qubit time evolution can clearly be extracted despite experimental shortcomings. With the current progress in superconducting-qubit technology, we expect that our understanding and the fidelity of available quantum computers to increase rapidly, allowing for more complex experiments, in particular with more qubits.

Going beyond (quasi)periodic driving, the capability to engineer time-dependent many-body Hamiltonians offers many exciting perspectives to investigate non-equilibrium physics.

For example, ramping through a quantum phase transition might allow one to study Kibble-Zurek scaling or in general the dynamics of phase transitions such as the superfluid to Mott insulator transition [49]. Slow variation could also be used to explore adiabatic algorithms and departures from them. Many-body non-equilibrium physics is notoriously difficult to study with classical computers and this is therefore a prime area of applicability for quantum simulators. Noisy intermediate-scale quantum computers offer a versatile combination of single-site control and readout, and large enough system sizes, and thus promise to support and complement analytical and computational approaches to understand many-body non-equilibrium physics. As we have demonstrated with the single-qubit experiment, this is a realistic outlook.

ACKNOWLEDGMENTS

DM acknowledges funding from ERC Advanced Grant QENOCOBA under the EU Horizon 2020 program (Grant Agreement No. 742102). AS was supported by the European Research Council (ERC) under the European Union’s Horizon 2020 research and innovation program (grant agreement No. 771537). The views expressed are those of the authors and do not reflect the official policy or position of IBM or the IBM Quantum Experience team.

DATA AVAILABILITY

All of the data presented in this paper, along with the python code used to generate this data and the figures in this paper, can be found in a public GitHub repository [50].

Appendix A: Qubit array Hamiltonian

1. Fixed qubit frequencies and fixed coupling

If neither the qubit frequencies nor the coupling between them is tuneable, the interaction Hamiltonian is time-independent. Restricting directly to the qubit subspace and assuming capacitive coupling for simplicity, we have

$$H(t) = \sum_i \omega_i \sigma_z^{(i)} + D_i(t) \sigma_x^{(i)} + J_{ij} \sum_{\langle ij \rangle} \sigma_x^{(i)} \sigma_x^{(j)}. \quad (\text{A1})$$

If the coupling J_{ij} is weak compared to the relative detuning, the qubits are effectively decoupled. Coupling between the i^{th} and j^{th} qubit can be turned on by driving either one at the frequency of the detuning between them [40, 41].

To see this, let us pass to the frame rotating with the qubit frequencies, and neglect terms rotating at the qubit frequency, which yields

$$H_{\text{RWA}}(t) = \sum_i d_i(t) \sigma_+^{(i)} + \sum_{\langle ij \rangle} J_{ij} \sigma_+^{(i)} \sigma_-^{(j)} e^{i(\omega_i - \omega_j)t} + \text{H.c.}, \quad (\text{A2})$$

where we parametrize the drive in two steps

$$\begin{aligned} D_i(t) &= 2 \text{Re} [d_i(t) e^{-i\omega_i t}] \\ &= 2 \text{Re} \left[d_i^{(0)}(t) e^{-i\omega_i t} + \sum_j \frac{\Delta_{ij}}{2J_{ij}^*} g_{ij}(t) e^{-i\omega_j t} \right], \end{aligned} \quad (\text{A3})$$

where $d_i^{(0)}(t), g_{ij}(t)$ are slow functions (compared to the coupling rate), we have defined the qubit-qubit detuning $\Delta_{ij} = \omega_i - \omega_j$ and the sum over j is taken to run over coupling qubits for which $J_{ij} \neq 0$.

We can now separate the Hamiltonian into a slow and a fast part. The slow Hamiltonian corresponds to the single-qubit Hamiltonian derived in the main text Eq. (5), except for many qubits

$$H_{\text{slow}} = \sum_i d_i^{(0)}(t) \sigma_+^{(i)} + \text{H.c.} \quad (\text{A4})$$

The fast part is off-resonant and has little effect, except when there are resonant processes. For example, to second order, the hopping becomes resonant again, leading to an Ising term of order $|J_{ij}|^2/\Delta_{ij}$. Since our original assumption is that the coupling is weak compared to the detuning, $J_{ij} \ll \Delta_{ij}$, this is negligible. However, the other term that appears at second order, mixing the off-resonant drive g_{ij} with the hopping J_{ij} is not negligible and in fact gives rise to the interaction

$$H_{\text{int}}^{(2)} = \sum_{\langle ij \rangle} g_{ij}(t) \sigma_z^{(i)} \sigma_+^{(j)} + \text{H.c.} \quad (\text{A5})$$

Combining Eqs. (A4) and (A5) allows one to engineer a wide range of time-dependent Hamiltonians. Note that due to drive enabling a resonant interaction between coupled qubits, the disorder has disappeared. The disorder can be restored by detuning the “coupling drive” $g_{ij}(t) = \exp(i \int^t h_z^{(j)}(t') dt') \tilde{g}_{ij}(t)$ and performing the same transformation on the single-qubit drives $d_i^{(0)}(t) = \exp(i \int^t h_z^{(i)}(t') dt') \tilde{d}_i^{(0)}(t)$, which in a rotating frame with respect to $H_z = \sum_i h_z^{(i)} \sigma_z^{(i)}$ reads

$$H = \sum_i \vec{h}_i(t) \cdot \vec{\sigma}_i + \sum_{\langle ij \rangle} \tilde{g}_{ij}^x(t) \sigma_z^{(i)} \sigma_x^{(j)} + \tilde{g}_{ij}^y(t) \sigma_z^{(i)} \sigma_y^{(j)} \quad (\text{A6})$$

with

$$\tilde{g}_{ij}(t) = \frac{1}{2} [\tilde{g}_{ij}^x(t) - i \tilde{g}_{ij}^y(t)], \quad (\text{A7})$$

The induced coupling is rich, as we have independently controllable XZ , ZX , YZ , and ZY interactions. If the qubit coupling graph is bipartite, i.e., if it can be separated into two subgraphs A and B such that nodes from A are only connect to B and vice versa, as for example in a square lattice, we can make a unitary transformation on every qubit one of the sublattices (B , say) that rotates Z into X and X into $-Z$. This allows us to engineer two particularly important interactions

- (i) We only have coupling XZ , with X on the A lattice and Z on the B lattice. After the unitary transformation, the coupling is XX . Similarly, starting from the coupling ZX , one obtains ZZ .

(ii) We employ both XZ and ZX . The unitary transformation yields $g_1XX + g_2ZZ$, or equivalently $g_1XX + g_2YY$.

Finally, we note that the biggest limitation for the controllability of this setup is an effect similar to *frequency crowding*. As this approach requires one to apply a range of different control tones at different frequencies, unwanted resonances can occur, which may affect the final effective Hamiltonian for the system. This problem particularly concerns lattices with high connectivity, but can typically be avoided by careful consideration and design of the applied tones.

2. Tuneable frequencies, but fixed interaction

If the qubit frequencies are tuneable, all the techniques from the previous section can be employed, but one gains the additional capacity to preclude frequency crowding.

In addition, one can make use of the direct interaction of the qubits by bringing them close to resonance. This realizes an XY interaction with tuneable disorder.

$$H = \sum_i h_z^{(i)} \sigma_z + \sum_{\langle ij \rangle} J_{ij} (\sigma_+^{(i)} \sigma_-^{(j)} + \text{H.c.}) \quad (\text{A8})$$

3. Tuneable interactions

For a set of qubits that interact via a tuneable XY interaction, the full Hamiltonian reads

$$H(t) = \sum_i \omega_i a_i^\dagger a_i + U_i a_i^\dagger a_i^\dagger a_i a_i + (a_i + a_i^\dagger) D_i(t) + \sum_{\langle ij \rangle} g_{ij}(t) (a_i^\dagger a_j + a_j^\dagger a_i), \quad (\text{A9})$$

Parameterizing the drive as before in terms of an effective magnetic field $\vec{h}_i(t)$, passing to a rotating frame with respect to the Hamiltonian $H_0 = \sum_i (\omega_0 - h_z^{(i)}(t)) a_i^\dagger a_i$ and restricting to the qubit subspace, we find

$$H(t) = \sum_i (\omega_i - \omega_0 + h_z^{(i)}(t)) \sigma_z^{(i)} + \left\{ \frac{1}{2} \sigma_-^{(i)} h_+^{(i)}(t) + \sum_{\langle ij \rangle} g_{ij}(t) \sigma_+^{(i)} \sigma_-^{(j)} e^{2i \int_0^t [h_z^{(j)}(t') - h_z^{(i)}(t')] dt'} + \text{H.c.} \right\} \quad (\text{A10})$$

Choosing $h_z^{(i)}(t) = h_z(t)$ for all i removes the phase on the interaction terms. The resulting Hamiltonian is

$$H(t) = \sum_i h_x^{(i)}(t) \sigma_x^{(i)} + h_y^{(i)}(t) \sigma_y^{(i)} + [h_z(t) + \delta_i] \sigma_z^{(i)} + \sum_{\langle ij \rangle} g_{ij}(t) [\sigma_x^{(i)} \sigma_x^{(j)} + \sigma_y^{(i)} \sigma_y^{(j)}]. \quad (\text{A11})$$

This is the Hamiltonian quoted in the main text. The disorder in the energies is inherited from the intrinsic disorder of the platform.

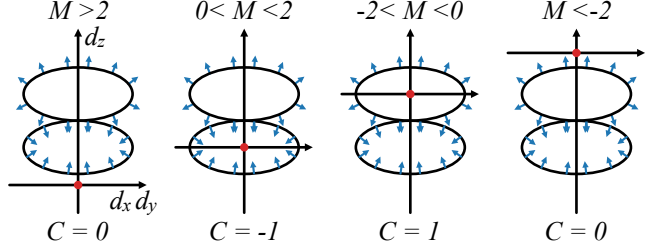


FIG. 3. Schematic of surface generated by the map $\vec{h}(\vec{k})$ from the Brillouin zone. A two-dimensional cross-section in corresponding to constant k_x or k_y is shown for simplicity. The normal to the surface is indicated by the blue arrows and the origin is highlighted in red.

Appendix B: Brief review of the BHZ model

The Bernevig-Hughes-Zhang (BHZ) is one of the simplest models for a two-dimensional Chern insulator [1]. It is a two-band lattice model that is most conveniently described in momentum space by the Hamiltonian

$$\hat{H}(\vec{k}) = \sin(k_x) \hat{\sigma}_x + \sin(k_y) \hat{\sigma}_y + B [M - \cos(k_x) - \cos(k_y)] \hat{\sigma}_z. \quad (\text{B1})$$

This Hamiltonian has the form $\hat{H}(\vec{k}) = \vec{h}(\vec{k}) \cdot \vec{\sigma} = \sum_a h_a(\vec{k}) \hat{\sigma}_a$, and spectrum given by $\lambda_{\pm} = \pm |\vec{h}|$, or more explicitly,

$$\lambda_{\pm} = \pm \sqrt{\sin^2(k_x) + \sin^2(k_y) + B^2 [M - \cos(k_x) - \cos(k_y)]^2} \quad (\text{B2})$$

which is gapped except at $M = -2, 0, 2$. Depending on the value of M this model realizes three different phases with these gap closings marking the phase transitions between them. For $|M| > 2$ we have a trivial insulator. For $-2 < M < 0$, we have Chern insulator with Chern number $C = +1$, and $0 < M < 2$ describes a Chern insulator with $C = -1$.

The eigenstates for the upper and lower band have the particularly simple form

$$|\psi_{\pm}\rangle = \frac{1}{\sqrt{2h(h \pm h_z)}} \begin{pmatrix} h \pm h_z \\ h_x + ih_y \end{pmatrix}, \quad (\text{B3})$$

which correspond to vectors on the Bloch sphere (anti-)aligned with the field direction \vec{h} . This can easily be seen by considering the vector of expectation values $\langle \vec{\sigma} \rangle = \pm \vec{h}/h$.

1. Chern number

To compute the Chern number we require the Berry connection $A_i(\vec{k})$ and/or the Berry curvature $F_{ij}(\vec{k})$, defined by

$$A_i(\vec{k}) = \sum_{\psi \in \text{filled bands}} -i \langle \psi | \frac{\partial}{\partial k_i} | \psi \rangle, \quad (\text{B4})$$

$$F_{ij}(\vec{k}) = \frac{\partial A_j}{\partial k_i} - \frac{\partial A_i}{\partial k_j}.$$

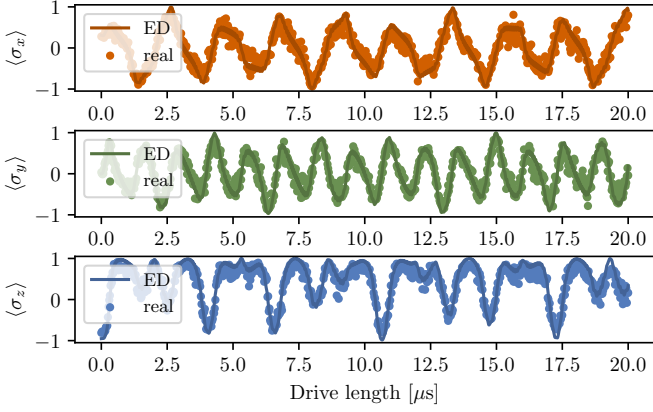


FIG. 4. Raw data from state tomography, shown as expectation values of the three Pauli operators. Data is for $M = 1$ and $\omega_1 = 0.125$ for 800 point in time and corresponds to that shown in Fig. 1. The solid curve is an exact numerical simulation and the circular markers are the raw experimental data.

The Chern number $C \in \mathbb{Z}$ is then computed by integrating the Berry curvature over the Brillouin zone:

$$C = \frac{1}{2\pi} \iint_{B.Z.} dk_x dk_y F_{xy}(\vec{k}). \quad (B5)$$

For the two-band model, the Berry curvature has a particularly intuitive form, namely

$$F_{xy}(\vec{k}) = \frac{1}{2h^3} \epsilon^{abc} h_a \partial_{k_x} h_b \partial_{k_y} h_c = \frac{1}{2h^3} \vec{h} \cdot (\partial_{k_x} \vec{h} \times \partial_{k_y} \vec{h}). \quad (B6)$$

The vector \vec{h} defines a map from the torus (B.Z.) to a two-dimensional surface M embedded in three dimensions. The Berry curvature then corresponds to the dot product of a field due to a unit charge at the origin and the normal of the surface S . The Chern number therefore measures the flux through the surface S , that is

$$C = \frac{1}{4\pi} \iint_M \frac{\vec{h}}{h^3} \cdot d\hat{S}, \quad (B7)$$

which measures the degree of map defined by \vec{h} , or equivalently, the winding of the surface M around the origin.

The surface prescribed by $\vec{h}(\vec{k})$ is closed self-intersecting surface with two lobes. the upper (along z -axis) lobe has normal facing outward, while lower has inward facing normal. The parameter M controls the position of this surface along the z -axis. The three phases therefore correspond to when the origin falls outside of the surface, or within one of the two lobes. This is shown schematically using a two-dimensional cross section in Fig. 3. Given this interpretation we can see that when $|M| > 2$ the Chern number must be zero since h_z does not change sign.

Appendix C: Measuring the work done by each drive

The computation of the work done by each drive proceeds by three main steps: i) state tomography, to obtain the spin

expectation values $\langle \vec{\sigma} \rangle$ at each time; ii) compute the expectation value $\langle dh_i/dt \rangle$; iii) numerically integrate Eq. (12) to get the work done by each drive.

To perform state tomography we run the experiment three times (with 8192 shots each) and measure the qubit in the X , Y and Z basis. We take the computational or natural basis for the qubit to be the Z basis. Each measurement gives an outcome of 0 or 1 corresponding to the eigenstates of the Pauli- Z operator with positive (+1) and negative (-1) eigenvalues, respectively. By averaging over the 8192 shots we obtain the average expectation value $\langle Z \rangle$, with standard error of the mean $2/\sqrt{8192} \sim 2\%$. To measure in the X basis we apply a Hadamard gate before measuring the qubit, and for the Y basis we apply an S^\dagger gate and a Hadamard gate before measuring. We then move to the rotating frame using Eq. (14). Fig. 4 shows an example of the measured Pauli expectation values corresponding to the data shown in Fig. 1 (i.e., $M = 1$) compared with the exact numerical simulation. The measured expectation values will not in general be consistent with a pure state due to a range of factors including statistical errors, measurement errors, and decoherence. We therefore normalize the vector of expectation values $\langle \vec{\sigma} \rangle$, which corresponds to projecting onto the Bloch sphere.

From this projected tomography data we can then compute the expectation values $\langle dh_i/dt \rangle = d\vec{h}_i/dt \cdot \langle \vec{\sigma} \rangle$, where

$$\begin{aligned} \frac{d\vec{h}_1}{dt} &= \eta \omega_1 \cos(\omega_1 t + \phi_1) \hat{x} + \eta \omega_1 \sin(\omega_1 t + \phi_1) \hat{z}, \\ \frac{d\vec{h}_2}{dt} &= \eta \omega_2 \cos(\omega_2 t + \phi_2) \hat{y} + \eta \omega_2 \sin(\omega_2 t + \phi_2) \hat{z}, \end{aligned} \quad (C1)$$

where, e.g. $\hat{x} \cdot \langle \vec{\sigma} \rangle = \langle \sigma_x \rangle$. In Fig. 5 we show the expectation values computed from the Pauli expectation values shown in Fig. 4, corresponding to Fig. 1 of the main text.

The final step is to numerically integrate these expectation values to get the work done by each drive, as given in Eq. (12). We use a simple trapezoid rule using data sampled at 800 points in time to 20 μ s.

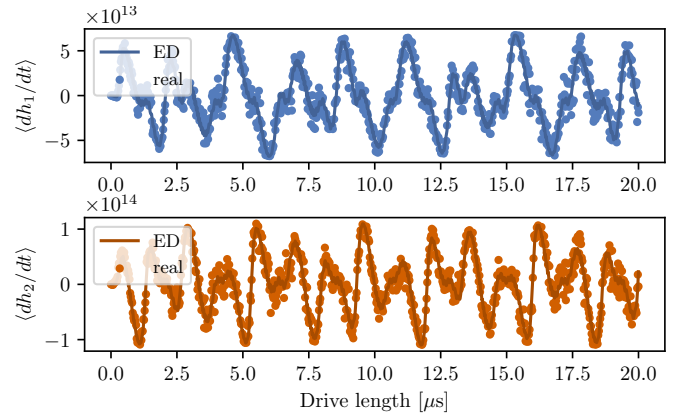


FIG. 5. Expectation values of $\langle dh_i/dt \rangle$ computed from the projected tomographic data shown in Fig. 4. The experimental data (circular markers) are compared with exact numerical simulations (solid lines).

In Fig. 6 we show the data from which we extracted the

work done by the drives to produce Fig. 2.

[1] J. Preskill, Quantum Computing in the NISQ era and beyond, *Quantum* **2**, 79 (2018), [arXiv:1801.00862](#).

[2] M. A. Nielsen and I. L. Chuang, *Cambridge Univ. Press.* (Cambridge University Press, Cambridge, 2010).

[3] A. Kandala, A. Mezzacapo, K. Temme, M. Takita, M. Brink, J. M. Chow, and J. M. Gambetta, Hardware-efficient variational quantum eigensolver for small molecules and quantum magnets, *Nature* **549**, 242 (2017).

[4] Y. Cao, J. Romero, J. P. Olson, M. Degroote, P. D. Johnson, M. Kieferová, I. D. Kivlichan, T. Menke, B. Peropadre, N. P. D. Sawaya, S. Sim, L. Veis, and A. Aspuru-Guzik, Quantum Chemistry in the Age of Quantum Computing, *Chemical Reviews* **119**, 10856 (2019).

[5] S. Lloyd, Universal Quantum Simulators, *Science* **273**, 1073 (1996).

[6] A. Smith, B. Jobst, A. G. Green, and F. Pollmann, Crossing a topological phase transition with a quantum computer, *1*, 1 (2019), [arXiv:1910.05351](#).

[7] F. Tacchino, A. Chiesa, S. Carretta, and D. Gerace, Quantum computers as universal quantum simulators: state-of-art and perspectives, (2019), [arXiv:1907.03505](#).

[8] A. Chiesa, F. Tacchino, M. Grossi, P. Santini, I. Tavernelli, D. Gerace, and S. Carretta, Quantum hardware simulating four-dimensional inelastic neutron scattering, *Nat. Phys.*, **15**, 455 (2019).

[9] F. Arute, K. Arya, R. Babbush, D. Bacon, J. C. Bardin, R. Barends, A. Bengtsson, S. Boixo, M. Broughton, B. B. Buckley, D. A. Buell, B. Burkett, N. Bushnell, Y. Chen, Z. Chen, Y.-A. Chen, B. Chiaro, R. Collins, S. J. Cotton, W. Courtney, S. Demura, A. Derk, A. Dunsworth, D. Eppens, T. Eckl, C. Erickson, E. Farhi, A. Fowler, B. Foxen, C. Gidney, M. Giustina, R. Graff, J. A. Gross, S. Habegger, M. P. Harrigan, A. Ho, S. Hong, T. Huang, W. Huggins, L. B. Ioffe, S. V. Isakov, E. Jeffrey, Z. Jiang, C. Jones, D. Kafri, K. Kechedzhi, J. Kelly, S. Kim, P. V. Klimov, A. N. Korotkov, F. Kostritsa, D. Landhuis, P. Laptev, M. Lindmark, E. Lucero, M. Marthaler, O. Martin, J. M. Martinis, A. Marusczyk, S. McArdle, J. R. McClean, T. McCourt, M. McEwen, A. Megrant, C. Mejuto-Zaera, X. Mi, M. Mohseni, W. Mruczkiewicz, J. Mutus, O. Naaman, M. Neeley, C. Neill, H. Neven, M. Newman, M. Y. Niu, T. E. O'Brien, E. Ostby, B. Pató, A. Petukhov, H. Putterman, C. Quintana, J.-M. Reiner, P. Roushan, N. C. Rubin, D. Sank, K. J. Satzinger, V. Smelyanskiy, D. Strain, K. J. Sung, P. Schmidteckert, M. Szalay, N. M. Tubman, A. Vainsencher, T. White, N. Vogt, Z. J. Yao, P. Yeh, A. Zalcman, and S. Zanker, Observation of separated dynamics of charge and spin in the Fermi-Hubbard model, (2020), [arXiv:2010.07965](#).

[10] P. Krantz, M. Kjaergaard, F. Yan, T. P. Orlando, S. Gustavsson, and W. D. Oliver, A quantum engineer's guide to superconducting qubits, *Applied Physics Reviews* **6**, 021318 (2019).

[11] S. Schmidt and J. Koch, Circuit QED lattices: Towards quantum simulation with superconducting circuits, *Annalen der Physik* **525**, 395 (2013).

[12] P. Roushan, C. Neill, A. Megrant, Y. Chen, R. Babbush, R. Barends, B. Campbell, Z. Chen, B. Chiaro, A. Dunsworth, A. Fowler, E. Jeffrey, J. Kelly, E. Lucero, J. Mutus, P. J. J. O'Malley, M. Neeley, C. Quintana, D. Sank, A. Vainsencher, J. Wenner, T. White, E. Kapit, H. Neven, and J. Martinis, Chiral ground-state currents of interacting photons in a synthetic magnetic field, *Nature Physics* **13**, 146 (2017).

[13] P. Roushan, C. Neill, J. Tangpanitanon, V. M. Bastidas, A. Megrant, R. Barends, Y. Chen, Z. Chen, B. Chiaro, A. Dunsworth, A. Fowler, B. Foxen, M. Giustina, E. Jeffrey, J. Kelly, E. Lucero, J. Mutus, M. Neeley, C. Quintana, D. Sank, A. Vainsencher, J. Wenner, T. White, H. Neven, D. G. Angelakis, and J. Martinis, Spectroscopic signatures of localization with interacting photons in superconducting qubits, *Science* **358**, 1175 (2017).

[14] B. Chiaro, C. Neill, A. Bohrdt, M. Filippone, F. Arute, K. Arya, R. Babbush, D. Bacon, J. Bardin, R. Barends, S. Boixo, D. Buell, B. Burkett, Y. Chen, Z. Chen, R. Collins, A. Dunsworth, E. Farhi, A. Fowler, B. Foxen, C. Gidney, M. Giustina, M. Harrigan, T. Huang, S. Isakov, E. Jeffrey, Z. Jiang, D. Kafri, K. Kechedzhi, J. Kelly, P. Klimov, A. Korotkov, F. Kostritsa, D. Landhuis, E. Lucero, J. McClean, X. Mi, A. Megrant, M. Mohseni, J. Mutus, M. McEwen, O. Naaman, M. Neeley, M. Niu, A. Petukhov, C. Quintana, N. Rubin, D. Sank, K. Satzinger, A. Vainsencher, T. White, Z. Yao, P. Yeh, A. Zalcman, V. Smelyanskiy, H. Neven, S. Gopalakrishnan, D. Abanin, M. Knap, J. Martinis, and P. Roushan, Direct measurement of non-local interactions in the many-body localized phase, (2019), [arXiv:1910.06024](#).

[15] Y. Yanay, J. Braumüller, S. Gustavsson, W. D. Oliver, and C. Tahan, Two-dimensional hard-core Bose-Hubbard model with superconducting qubits, *npj Quantum Information* **6**, 58 (2020).

[16] I. Martin, G. Refael, and B. Halperin, Topological Frequency Conversion in Strongly Driven Quantum Systems, *Physical Review X* **7**, 041008 (2017).

[17] B. A. Bernevig, T. L. Hughes, and S.-C. Zhang, Quantum Spin Hall Effect and Topological Phase Transition in HgTe Quantum Wells, *Science* **314**, 1757 (2006).

[18] P. J. D. Crowley, I. Martin, and A. Chandran, Topological classification of quasiperiodically driven quantum systems, *Physical Review B* **99**, 064306 (2019).

[19] F. Nathan, G. Refael, M. S. Rudner, and I. Martin, Quantum phase-locking and frequency down-conversion in a driven cavity-qubit system, (2020), [arXiv:2003.05648](#).

[20] S. Körber, L. Privitera, J. C. Budich, and B. Trauzettel, Interacting topological frequency converter, *Physical Review Research* **2**, 022023 (2020).

[21] Y. Baum and G. Refael, Setting Boundaries with Memory: Generation of Topological Boundary States in Floquet-Induced Synthetic Crystals, *Physical Review Letters* **120**, 106402 (2018).

[22] T. Alexander, N. Kanazawa, D. J. Egger, L. Capelluto, C. J. Wood, A. Javadi-Abhari, and D. McKay, Qiskit Pulse: Programming Quantum Computers Through the Cloud with Pulses, (2020), [arXiv:2004.06755](#).

[23] A. Eckardt, Colloquium: Atomic quantum gases in periodically driven optical lattices, *Reviews of Modern Physics* **89**, 011004 (2017).

[24] T. Oka and S. Kitamura, Floquet Engineering of Quantum Materials, *Annual Review of Condensed Matter Physics* **10**, 387 (2019).

[25] T. Ozawa and H. M. Price, Topological quantum matter in syn-

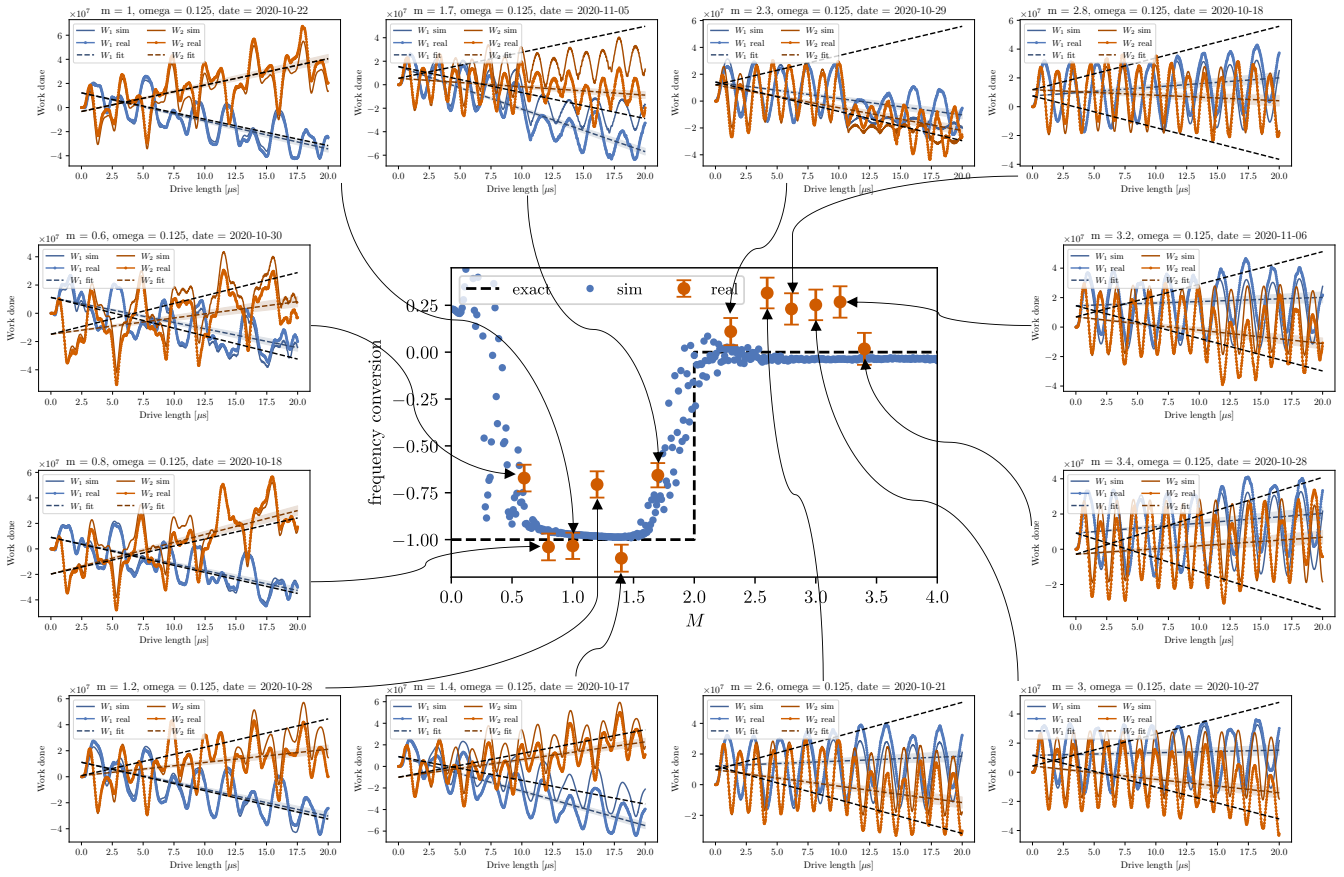


FIG. 6. Plots of the work done by the two drives and their linear fits for each of the data points shown in Fig. 2, as discussed in Appendix C.

thetic dimensions, *Nature Reviews Physics* **1**, 349 (2019).

[26] T. Ozawa, H. M. Price, A. Amo, N. Goldman, M. Hafezi, L. Lu, M. C. Rechtsman, D. Schuster, J. Simon, O. Zilberberg, and I. Carusotto, Topological photonics, *Reviews of Modern Physics* **91**, 015006 (2019).

[27] V. Khemani, R. Moessner, and S. L. Sondhi, A Brief History of Time Crystals, (2019), [arXiv:1910.10745](https://arxiv.org/abs/1910.10745).

[28] C. Noh and D. G. Angelakis, Quantum simulations and many-body physics with light, *Reports on Progress in Physics* **80**, 016401 (2017).

[29] I. Bloch, J. Dalibard, and S. Nascimbène, Quantum simulations with ultracold quantum gases, *Nature Physics* **8**, 267 (2012).

[30] J. Koch, T. M. Yu, J. Gambetta, A. A. Houck, D. I. Schuster, J. Majer, A. Blais, M. H. Devoret, S. M. Girvin, and R. J. Schoelkopf, Charge-insensitive qubit design derived from the Cooper pair box, *Physical Review A* **76**, 042319 (2007).

[31] M. Kjaergaard, M. E. Schwartz, J. Braumüller, P. Krantz, J. I.-J. Wang, S. Gustavsson, and W. D. Oliver, Superconducting Qubits: Current State of Play, (2019), [arXiv:1905.13641](https://arxiv.org/abs/1905.13641).

[32] D. C. McKay, C. J. Wood, S. Sheldon, J. M. Chow, and J. M. Gambetta, Efficient Z gates for quantum computing, *Physical Review A* **96**, 1 (2017).

[33] A. Blais, R.-S. Huang, A. Wallraff, S. M. Girvin, and R. J. Schoelkopf, Cavity quantum electrodynamics for superconducting electrical circuits: An architecture for quantum computation, *Physical Review A* **69**, 062320 (2004).

[34] Y. X. Liu, L. F. Wei, J. S. Tsai, and F. Nori, Controllable coupling between flux qubits, *Physical Review Letters* **96**, 1 (2006).

[35] A. O. Niskanen, K. Harrabi, F. Yoshihara, Y. Nakamura, S. Lloyd, and J. S. Tsai, Quantum coherent tunable coupling of superconducting qubits, *Science* **316**, 723 (2007).

[36] M. S. Allman, F. Altomare, J. D. Whittaker, K. Cicak, D. Li, A. Sirois, J. Strong, J. D. Teufel, and R. W. Simmonds, rf-SQUID-Mediated Coherent Tunable Coupling between a Superconducting Phase Qubit and a Lumped-Element Resonator, *Physical Review Letters* **104**, 177004 (2010).

[37] S. J. Srinivasan, A. J. Hoffman, J. M. Gambetta, and A. A. Houck, Tunable coupling in circuit quantum electrodynamics using a superconducting charge qubit with a V-Shaped energy level diagram, *Physical Review Letters* **106**, 1 (2011).

[38] A. Kandala, K. Temme, A. D. Córcoles, A. Mezzacapo, J. M. Chow, and J. M. Gambetta, Error mitigation extends the computational reach of a noisy quantum processor, *Nature* **567**, 491 (2019).

[39] Y. Chen, C. Neill, P. Roushan, N. Leung, M. Fang, R. Barends, J. Kelly, B. Campbell, Z. Chen, B. Chiaro, A. Dunsworth, E. Jeffrey, A. Megrant, J. Y. Mutus, P. J. J. O’Malley, C. M. Quintana, D. Sank, A. Vainsencher, J. Wenner, T. C. White, M. R. Geller, A. N. Cleland, and J. M. Martinis, Qubit Architecture with High Coherence and Fast Tunable Coupling, *Physical Review Letters* **113**, 220502 (2014).

[40] G. S. Paraoanu, Microwave-induced coupling of superconducting qubits, *Physical Review B* **74**, 140504 (2006).

[41] C. Rigetti and M. Devoret, Fully microwave-tunable universal gates in superconducting qubits with linear couplings and fixed transition frequencies, *Physical Review B* **81**, 134507 (2010).

[42] P. C. De Groot, J. Lisenfeld, R. N. Schouten, S. Ashhab, A. Lupaşcu, C. J. Harmans, and J. E. Mooij, Selective darkening of degenerate transitions demonstrated with two superconducting quantum bits, *Nature Physics* **6**, 763 (2010).

[43] S. Sheldon, E. Magesan, J. M. Chow, and J. M. Gambetta, Procedure for systematically tuning up cross-talk in the cross-resonance gate, *Physical Review A* **93**, 060302 (2016).

[44] L. DiCarlo, J. M. Chow, J. M. Gambetta, L. S. Bishop, B. R. Johnson, D. I. Schuster, J. Majer, A. Blais, L. Frunzio, S. M. Girvin, and R. J. Schoelkopf, Demonstration of two-qubit algorithms with a superconducting quantum processor, *Nature* **460**, 240 (2009).

[45] R. Barends, J. Kelly, A. Megrant, A. Veitia, D. Sank, E. Jeffrey, T. C. White, J. Mutus, A. G. Fowler, B. Campbell, Y. Chen, Z. Chen, B. Chiaro, A. Dunsworth, C. Neill, P. O’Malley, P. Roushan, A. Vainsencher, J. Wenner, A. N. Korotkov, A. N. Cleland, and J. M. Martinis, Superconducting quantum circuits at the surface code threshold for fault tolerance, *Nature* **508**, 500 (2014).

[46] J. Kelly, R. Barends, A. G. Fowler, A. Megrant, E. Jeffrey, T. C. White, D. Sank, J. Y. Mutus, B. Campbell, Y. Chen, Z. Chen, B. Chiaro, A. Dunsworth, I.-C. Hoi, C. Neill, P. J. J. O’Malley, C. Quintana, P. Roushan, A. Vainsencher, J. Wenner, A. N. Cleland, and J. M. Martinis, State preservation by repetitive error detection in a superconducting quantum circuit, *Nature* **519**, 66 (2015).

[47] M. Reagor, C. B. Osborn, N. Tezak, A. Staley, G. Prawiroatmodjo, M. Scheer, N. Alidoust, E. A. Sete, N. Didier, M. P. da Silva, E. Acala, J. Angeles, A. Bestwick, M. Block, B. Bloom, A. Bradley, C. Bui, S. Caldwell, L. Capelluto, R. Chilcott, J. Cordova, G. Crossman, M. Curtis, S. Deshpande, T. El Bouayadi, D. Girshovich, S. Hong, A. Hudson, P. Karalekas, K. Kuang, M. Lenihan, R. Manenti, T. Manning, J. Marshall, Y. Mohan, W. O’Brien, J. Otterbach, A. Pappa-george, J.-P. Paquette, M. Pelstring, A. Polloreno, V. Rawat, C. A. Ryan, R. Renzas, N. Rubin, D. Russel, M. Rust, D. Scarabelli, M. Selvanayagam, R. Sinclair, R. Smith, M. Suska, T. W. To, M. Vahidpour, N. Vodrahalli, T. Whyland, K. Yadav, W. Zeng, and C. T. Rigetti, Demonstration of universal parametric entangling gates on a multi-qubit lattice, *Science Advances* **4**, eaao3603 (2018).

[48] D. C. McKay, S. Filipp, A. Mezzacapo, E. Magesan, J. M. Chow, and J. M. Gambetta, Universal Gate for Fixed-Frequency Qubits via a Tunable Bus, *Physical Review Applied* **6**, 064007 (2016).

[49] S. Braun, M. Friesdorf, S. S. Hodgman, M. Schreiber, J. P. Ronzheimer, A. Riera, M. del Rey, I. Bloch, J. Eisert, and U. Schneider, Emergence of coherence and the dynamics of quantum phase transitions, *Proceedings of the National Academy of Sciences* **112**, 3641 (2015).

[50] Daniel Malz, and Adam Smith, <https://github.com/as2457/qubit-topological-floquet>.